JOURNAL OF GUIDANCE, CONTROL, AND DYNAMICS
Vol. 34, No. 4, July–August 2011

Flight Control Experiment of Multipurpose-Aviation-Laboratory-α In-Flight Simulator

Masayuki Sato*
Japan Aerospace Exploration Agency, Mitaka, Tokyo 181-0015, Japan
and
Atsushi Satoh†
Iwate University, Morioka, Iwate 020-8551, Japan

DOI: 10.2514/1.52400

This paper reports the results of experimental verification of flight controllers for the multipurpose-aviation-laboratory-α (MuPAL-α) in-flight simulator. The flight controller design requirements are twofold: to suppress the effects of gusts on MuPAL-α motions and to realize a wide range of maneuverability, i.e., handling characteristics, without controller redesign. Using a previously proposed two-step design method for two-degrees-of-freedom model-matching controllers, flight controllers were designed for the linearized longitudinal and lateral-directional motions of MuPAL-α, and their performance was examined by hardware-in-the-loop simulations and flight tests with several maneuverability models. These experiments confirmed that MuPAL-α with our controllers achieves gust suppression and is capable of simulating various types of handling characteristics simply by replacing the model that defines the characteristics to be examined.

Nomenclature

A, B, C, D	=	matrices for state-space representation
$\mathsf{diag}(X_1, \cdots, X_k)$	=	block-diagonal matrix composed of $X_1, \cdots, X_k$
F	=	feedforward controller
$G(s)$	=	transfer function of system G
$\|G(s)\|_\infty$	=	H_∞ norm of system G
$\mathbf{I}$	=	appropriately dimensioned identity matrix
I_n	=	$n \times n$ dimensional identity matrix
K	=	feedback controller
L'_v, L'_{δ_a}	=	dimensional primed derivatives related to L-component
M	=	maneuverability dynamics of target aircraft model
M_u, M_w, M_{δ_e}	=	dimensional derivatives related to M-component
N'_v, N'_{δ_r}	=	dimensional primed derivatives related to N-component
P	=	plant dynamics
P_g	=	generalized plant for designing feedback controllers
P_n	=	nominal plant dynamics
p	=	roll rate
q	=	pitch rate
r	=	yaw rate
u_{fb}	=	feedback control input
u_{ff}	=	feedforward control input
u_i, u_a, u_g	=	forward-backward inertial velocity, air velocity, and gust velocity
u_m	=	handling input to target aircraft model
u_p	=	control input of plant
v_i, v_a, v_g	=	lateral inertial velocity, air velocity, and gust velocity
w_{gust}	=	wind gust input to plant
w_i, w_a, w_g	=	vertical inertial velocity, air velocity, and gust velocity
$\|X\|$	=	maximum singular value of matrix X
X_u, X_τ	=	dimensional derivatives related to X-component
Y_v, Y_{δ_r}	=	dimensional derivatives related to Y-component
y_p	=	measurement output of plant
$Z_w, Z_{\delta_e}, Z_{\delta_{\mathrm{DLC}}}$	=	dimensional derivatives related to Z-component
z_m	=	output of target aircraft model
z_p	=	controlled output of plant
δ_a, δ_{a_c}	=	aileron deflection and command
$\delta_{\mathrm{DLC}}, \delta_{\mathrm{DLC}_c}$	=	direct lift control flap deflection and command
δ_e, δ_{e_c}	=	elevator deflection and command
$\delta_{\mathrm{pl}}, \delta_{\mathrm{pl}_c}$	=	power lever deflection and command
δ_r, δ_{r_c}	=	rudder deflection and command
$\zeta(\omega)$	=	minimum gain of diagonal weighting function W_2 at frequency ω
θ	=	pitch angle
$\mu_\Delta(X)$	=	structured singular value of matrix X with structured uncertainty Δ
τ	=	engine torque
ϕ	=	roll angle
ψ	=	yaw angle
$\mathbf{0}$	=	appropriately dimensioned zero matrix

I. Introduction

ACCORDING to [1], the term *in-flight simulator* (IFS) describes an aircraft that achieves an extension of ground-based simulators to the flight environment and its real-world cues. Put simply, an IFS is an aircraft that can mimic another aircraft's characteristics, such as handling, gust response, and the operation of onboard equipment. This makes an IFS a useful tool for a range of aircraft research, including handling qualities investigation, avionics development, and special pilot training [1]. In particular, IFSs play a key role in evaluating the handling characteristics, i.e., maneuverability, of newly developed aircraft before actual first flight by mimicking the response of the aircraft to pilot control

Received 16 September 2010; revision received 30 January 2011; accepted for publication 8 February 2011.

*Researcher, Institute of Space Technology and Aeronautics, 6-13-1 Osawa; sato.masayuki@jaxa.jp.

†Associate Professor, Department of Mechanical Engineering; satsushi@iwate-u.ac.jp.

inputs [1,2]. For these reasons, many IFSs have been developed since the 1940s, e.g., the NASA F6F-3 [1], total in-flight simulator [1,3], variable stability in-flight simulator test aircraft [1], advanced technologies testing aircraft system [4,5], variable stability response aircraft [6], and multipurpose aviation laboratory α (MuPAL-α) [7]. The background and history of IFS development can be found in [1,8] and references therein.

Some IFSs use model-following flight controllers to realize desired maneuverability. In general, model-following controllers depend heavily on the dynamics of the target aircraft model,[‡] which means that if the target aircraft model is changed then the controller should also be redesigned. However, for the handling qualities assessment and basic flight control system development of a newly developed aircraft, it is highly desirable that the target aircraft maneuverability can be realized without IFS controller redesign, for the following reasons: handling qualities assessment and new aircraft developments often require the tuning of flight control system parameters, and it is preferable to conduct flight tests immediately after tuning in order to investigate the need for further tuning; and, ideally, all tests should be conducted during a single flight, so that test conditions are as similar as possible. These require an IFS flight controller that can simulate a wide range of maneuverability without redesign. Moreover, when the maneuverability of a target aircraft is to be examined in isolation, the effects of gust disturbance on IFS motions must be minimized.

IFS flight controllers that satisfy the following two design requirements are therefore desired: 1) suppression of the effects of gusts on IFS motions and 2) realization of a wide range of maneuverability without controller redesign.

Figure 1 shows the general block diagram of an IFS flight controller. z_p denotes the signal that characterizes the maneuverability to be realized (e.g., pitch angle, roll angle, etc.), and z_m denotes the corresponding signal for the target aircraft model. The first of the preceding requirements is equivalent to minimizing the effect of w_{gust} on z_p, and the second is equivalent to the reproduction of z_m as z_p for all possible u_m under $w_{\text{gust}} = \mathbf{0}$. If a flight controller satisfies both these requirements, then an IFS with the flight controller will realize the desired maneuverability of M while minimizing the effect of gusts on the IFS motions.

The authors previously proposed a design method for IFS flight controllers that satisfy the preceding two requirements using two-degrees-of-freedom (two-DOF) model-matching controllers, and confirmed that a controller designed for the lateral-directional motions of MuPAL-α, shown in Fig. 2, satisfied the requirements [9]. However, the method's applicability was confirmed only for lateral-directional motions.

This paper reports the results of experimental verification of flight controllers satisfying the preceding two requirements, for the longitudinal motions as well as the lateral-directional motions of MuPAL-α. The controllers are designed using the method in [9]. Three different aircraft models are used as the target aircraft model in experiments: a Boeing 747 (B747) model, a newly developed regional jet model, and an artificial aircraft model with highly unconventional dynamics. Using these models, we confirm that our controllers realize a wide range of maneuverability simply by substituting the target aircraft model rather than controller redesign.

The biggest differences between the longitudinal and lateral-directional motions in our problem are the number of disturbance inputs and the consequent difficulty of designing feedback controllers to achieve gust suppression. For lateral-directional motions, the only wind gust component is v_g, but for longitudinal motions wind gust has two components, u_g and w_g. Consequently, the number of transfer functions of which gains must be reduced for gust suppression is at least doubled for longitudinal motions, which increases the complexity of the design problem.

Furthermore, the suppression of a vertical velocity w_a induced by a vertical gust w_g is aerodynamically more difficult for MuPAL-α to achieve than suppression of a lateral velocity v_a induced by a lateral gust v_g, which has already been achieved in [9]. The reason for this is, briefly, as follows. The dimensional derivatives related to the gust suppression problem for the linearized motions of MuPAL-α are shown in Tables 1 and 2 (see also Sec. II for the details of our problem). Roughly speaking, for MuPAL-α to achieve gust suppression, its control devices must produce equal opposing forces or moments to those induced by wind gusts. If MuPAL-α encounters a 1 m/s vertical step gust w_g, either its elevator must deflect 12.23 deg, its direct lift control (DLC) flap must deflect 8.74 deg, or there must be some combination of these to cancel the force driven by the gust. On the other hand, if MuPAL-α encounters a 1 m/s horizontal step gust v_g, its rudder must deflect only 3.41 deg to cancel the gust force (Table 3 shows the required control deflections for step gusts). The required elevator and DLC flap deflections are much greater than the required rudder deflection for the same magnitude of gust, which means that the flight controller gains for longitudinal motions must be greater than those for lateral-directional motions. In

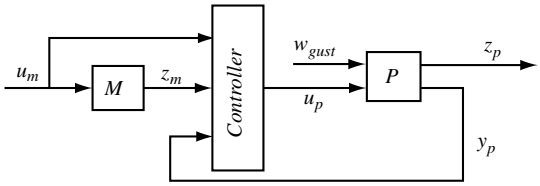

Fig. 1 General block diagram of an IFS flight controller.

Fig. 2 IFS MuPAL-α.

Table 1 Dimensional derivatives of longitudinal motions of MuPAL-α

Dimensional derivative	Value
X_u, 1/s	−0.019
X_τ, m/s^2/%	0.025
Z_w, 1/s	−1.155
Z_{δ_e}, m/s^2/rad	−5.41
$Z_{\delta_{\text{DLC}}}$, m/s^2/rad	−7.57
M_u, 1/m/s	0.006
M_w, 1/m/s	−0.083
M_{δ_e}, 1/s^2/rad	−4.61

Table 2 Dimensional derivatives of lateral-directional motions of MuPAL-α

Dimensional derivative	Value
Y_v, 1/s	−0.189
Y_{δ_r}, m/s^2/rad	3.18
L'_v, 1/m/s	−0.061
L'_{δ_a}, 1/s^2/rad	−11.80
N'_v, 1/m/s	0.028
N'_{δ_r}, 1/s^2/rad	−2.45

[‡]In this paper, the aircraft for which maneuverability is to be realized is referred to as the *target aircraft*, and the aircraft which implements the IFS system is referred to as the *IFS*.

Table 3 Control surface deflections required to suppress a 1 m/s gust

Component	Control surface deflection
	u_g
X	$\tau = -0.76$ %
M	$\delta_e = -0.07$ deg
	w_g
Z	$\delta_e = 12.23$ deg
Z	$\delta_{\mathrm{DLC}} = 8.74$ deg
M	$\delta_e = 1.03$ deg
	v_g
Y	$\delta_r = -3.41$ deg
L	$\delta_a = 0.30$ deg
N	$\delta_r = -0.65$ deg

general, high controller gains easily result in instability of closed-loop systems, and so lower gains are required to prevent this. However, lower gains reduce gust suppression performance.

For these reasons, gust suppression controller design for the longitudinal motions of MuPAL-α is more difficult than for its lateral-directional motions.

This paper is organized as follows. Section II reviews the controller structure adopted in this paper, then briefly reviews the design method in [9], and finally describes the details for designing the flight controllers for MuPAL-α. Section III describes hardware-in-the-loop (HIL) simulations and flight tests. Finally, Sec. IV presents concluding remarks.

II. Controller Design

A. Controller Structure

Figure 3a shows the block diagram of a well-known two-DOF controller structure. F_A and K_A, respectively, denote a feedforward controller element and a feedback controller element. It is assumed, for simplicity, that the plant measurement output is identical to z_p. This structure is widely used for tracking problems, in which M is set as $\mathbf{I}$ and u_m is set as the reference signal.

To meet the preceding design requirements, K_A is designed as an internally stabilizing and disturbance suppressing controller for the plant P, and F_A is designed as a feedforward controller that achieves model-matching for various M without considering either the stability or the gust suppression performance of the closed-loop system. One of the greatest merits of the two-DOF controller in Fig. 3a is that controllers F_A and K_A can be designed independently. When the plant P is unstable, F_A must be designed for the unstable plant. Linearized aircraft motion models are sometimes unstable, like the lateral-directional motions of MuPAL-α. Some modern control theories, e.g., linear quadratic optimal control theory and H_∞ control theory, suppose that the controlled system comprising the plant and controller to be designed is stabilized. However, this cannot be achieved when designing F_A for an unstable plant model P, because F_A has no effect on the internal stability of P; i.e., such control theories cannot be applied for the design of F_A. Alternatively, an inverse system of P can be designed as F_A using the methods in [10] or the references therein, which circumvents the stability problem of the connected system of P and F_A. However, this approach cannot be used if the plant has unstable zeros, because these lead to instability of the designed inverse systems. In summary, when using the structure in Fig. 3a, there are difficulties for designing F_A when P is unstable and/or nonminimum phase.

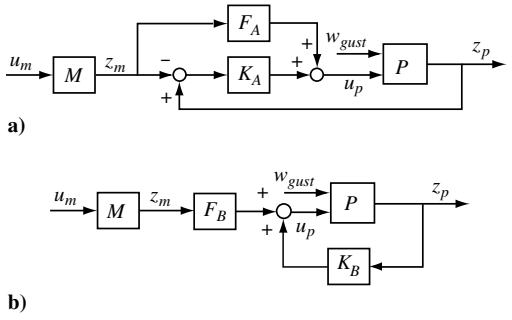

Fig. 3 Block diagram of two-DOF controller structure: a) general two-DOF controller and b) adopted two-DOF controller.

To circumvent these difficulties, we adopt an alternative two-DOF controller structure, shown in Fig. 3b. If K_B and F_B are, respectively, set as K_A and $F_A - K_A$, it is easily confirmed that the two-DOF controller (Fig. 3b) is identical to the two-DOF controller (Fig. 3a). However, there is a crucial difference when designing F_B; in this case, although the controller F_B should be designed after K_B, there is no difficulty in applying modern control theory when designing F_B, because, in general, K_B is designed as an internally stabilizing controller for plant P. The two-DOF controller structure (Fig. 3b) is, therefore, adopted as the IFS flight controller structure in this paper, and F_B is designed after K_B, similar to [9].

B. Design Method

The design methods for the feedback and feedforward controllers are reviewed only briefly next, because their details can be found in [9].

1. *Feedback Controller Design*

Suppose that the plant dynamics incorporating plant uncertainties are given. For plant dynamics P and a stable diagonal weighting function W_1 that defines the gust suppression performance of controller K, the generalized plant P_g for designing controller K is given as the connected system of P and W_1 (see Fig. 4). In Fig. 4, $w = [\, w_{\mathrm{gust}}^T \quad w_u^T \,]^T$ denotes the disturbance input of P_g comprising gust input w_{gust} and the uncertain block output w_u, and $z = [\, z_1^T \quad z_u^T \,]^T$ denotes the controlled output of P_g comprising the weighted performance output for gust suppression z_1 and the uncertain block input z_u.

The uncertainty is normalized and given as $\tilde{\Delta}_K := \mathsf{diag}(\Delta_u, \Delta_{p_K})(\|\tilde{\Delta}_K\| \le 1)$, in which Δ_u and Δ_{p_K}, respectively, denote an uncertainty block with respect to the plant uncertainties and a fictitious performance block (see Fig. 4).

For a diagonal weighting function W_1, in which all entries have sufficiently large gains in some frequency range, suppose that a feedback controller is designed that internally stabilizes the generalized plant P_g and satisfies the inequality

$$\sup_{\omega \in \mathcal{R}} \mu_{\tilde{\Delta}_K}(G_{zw}(j\omega)) < 1 \tag{1}$$

in which G_{zw} is the closed-loop system from w to z. Then, the gains of the controlled plant from w_{gust} to z_p become sufficiently small in the frequency range under the prescribed plant uncertainties. Thus, the design problem of feedback controller K for gust suppression is as follows.

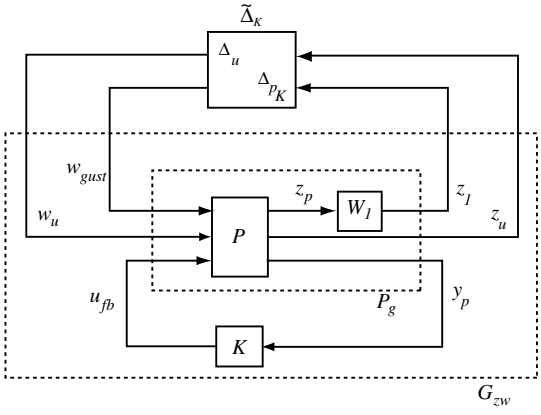

Fig. 4 Block diagram for design of feedback controller K.

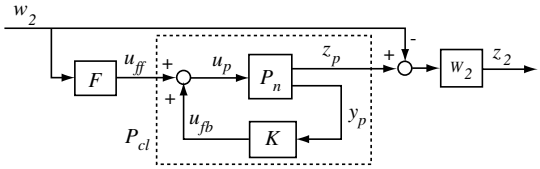

Fig. 5 Block diagram for design of feedforward controller F.

Problem 1: for an appropriately defined stable diagonal weighting function W_1, find a controller K that internally stabilizes P_g and satisfies Eq. (1).

This problem is a typical μ-synthesis, and, in general, it is very difficult to obtain the global optimal controller. We therefore have to design a suboptimal controller using heuristic algorithms, such as $D-K$ iteration.

2. *Feedforward Controller Design*

The feedforward controller is designed as a filtered right inverse system of the closed-loop system comprising the plant and the feedback controller. In sharp contrast to feedback controllers, feedforward controllers cannot diminish uncertainty effect. Although several methods have been proposed for the design of robust feedforward controllers, e.g., [11,12], they are not used in our design because they failed to give a controller with adequate inverse performance when we attempted to apply them. We therefore first design filtered right inverse systems for nominal plant models (i.e., plant uncertainties are not considered in the feedforward controller design), then check their robust performance against the uncertainties a posteriori. If controller performance is far from satisfying the design requirements, the feedforward controllers should be redesigned with reduced performance requirements.

The block diagram for designing feedforward controllers is shown in Fig. 5. Here, P_n denotes the nominal dynamics of the plant, with the gust input being eliminated; W_2 is a stable diagonal weighting function that specifies the right inverse performance and its frequency range; and w_2 and z_2, respectively, denote a fictitious disturbance input and a fictitious controlled output for filtered right inverse design problem [12].

If a designed stable feedforward controller F satisfies $\|G_{z_2w_2}(s)\|_\infty < 1$, in which $G_{z_2w_2}$ denotes the system from w_2 to z_2, then the following inequalities hold for $P_o = P_{\mathrm{cl}}F$, in which P_{cl} denotes the closed-loop system depicted in Fig. 5 [12]:

$$
\begin{aligned}
&|P_{o_{ll}}(j\omega) - 1| < 1/\zeta(\omega), \quad \forall\ l \\
&|\angle P_{o_{ll}}(j\omega)| < \arcsin 1/\zeta(\omega), \quad \forall\ l \\
&|P_{o_{lm}}| < 1/\zeta(\omega), \quad \forall\ l, m \qquad l \neq m
\end{aligned} \tag{2}
$$

in which $\zeta(\omega)(>1)$ is defined as the minimum gain of W_2 at frequency ω, and $P_{o_{lm}}$ denotes the (l, m) entry of P_o.

Table 4 Variables for MuPAL-α longitudinal motion

Variable	Element
State	$(u_i$ m/s $\quad w_i$ m/s $\quad q$ rad/s $\quad \theta$ rad $\quad \tau$ %$)^T$
Gust	$(u_g$ m/s $\quad w_g$ m/s$)^T$
Control input	$(\delta_e$ rad $\quad \delta_{\mathrm{DLC}}$ rad $\quad \delta_{\mathrm{pl}}$ mm$)^T$
Controlled output	$(u_a$ m/s $\quad w_a$ m/s $\quad \theta$ deg$)^T$
Measurement output	$(u_a$ m/s $\quad w_a$ m/s $\quad q$ rad/s $\quad \theta$ rad$)^T$

Table 5 Variables for MuPAL-α lateral-directional motion

Variable	Element
State	$(v_i$ m/s $\quad p$ rad/s $\quad \phi$ rad $\quad r$ rad/s$)^T$
Gust	v_g m/s
Control input	$(\delta_a$ rad $\quad \delta_r$ rad$)^T$
Controlled output	$(\phi$ deg $\quad r$ deg/s$)^T$
Measurement output	$(v_a$ m/s $\quad p$ rad/s $\quad \phi$ rad $\quad r$ rad/s$)^T$

This consequently means that the system described as $P_{\mathrm{cl}}F$ almost reproduces its input signal in the frequency range, in which $\zeta(\omega)$ is sufficiently large, as its output signal; i.e., in Fig. 3b, the IFS controller can realize various types of maneuverability in the frequency range simply by replacing the target aircraft model M.

The design problem of the feedforward controller F is given as follows.

Problem 2: for an appropriately defined stable diagonal weighting function W_2, find a stable controller F that satisfies $\|G_{z_2w_2}(s)\|_\infty < 1$.

If the controller is set as full order, which is the case with our design in the next subsection, then this problem is a standard H_∞ problem and is easily solved using standard software tools.

C. MuPAL-α Controllers

Flight controllers for the longitudinal and lateral-directional motions of MuPAL-α were designed using the methods described previously.

MuPAL-α has conventional controls: elevator and engine thrust are used for longitudinal motion control, supplemented by a DLC flap, and ailerons and rudder are used for lateral-directional motion control. Thus, the number of controlled outputs for the longitudinal and lateral-directional motions were set as three and two, respectively. The controlled outputs were set as $[u_a \quad w_a \quad \theta]^T$ for the longitudinal motions, and as $[\phi \quad r]^T$ for the lateral-directional motions.

1. *Plant Description*

The plant model is given as the linearized aircraft motion model of MuPAL-α at a true airspeed of $V_{\mathrm{TAS}} = 69.8$ m/s and an altitude of $H = 1520$ m. The state variables, etc., in the longitudinal and lateral-directional motions are given in Tables 4 and 5, respectively.

The linearized motion model of MuPAL-α faithfully represents its nonlinear motions around the equilibrium point, and uncertainties related to the linearization were not considered. On the other hand, the control actuator systems have uncertainties that are described next. Actuator dynamics models were constructed by investigating responses to step commands of several amplitudes and sinusoidal commands of several amplitudes and frequencies. Some typical time histories are shown in Figs. 6 and 7. These confirm the presence of some nonlinearities and uncertain factors such as backlash and variable dead time. To represent these, we used uncertain delays, i.e., dead time T_{delay} with $T_{\mathrm{delay}} \in [T_{\min}, T_{\max}]$, and supposed that actuator dynamics are represented as a serially connected system of a low-order (first- or zero-order) system and a delay model, i.e., $\frac{k}{T_c s+1} e^{-sT_{\mathrm{delay}}}$, when using a first-order system, in which k and T_c are, respectively, the gain and the time constant of the first-order system, or $ke^{-sT_{\mathrm{delay}}}$ when using a zero-order system, in which k is the gain of the zero-order system. From step and sinusoidal response data, the uncertain dead times were identified as follows:

$$
\begin{aligned}
&T_e \in [0.06, 0.36] \quad \text{(elevator)} \\
&T_{\mathrm{DLC}} \in [0.06, 0.20] \quad \text{(DLC flap)} \\
&T_{\mathrm{pl}} \in [0.06, 0.20] \quad \text{(power lever)} \\
&T_a \in [0.06, 0.40] \quad \text{(aileron)} \\
&T_r \in [0.06, 0.20] \quad \text{(rudder)}
\end{aligned} \tag{3}
$$

Using the uncertain dead times in Eq. (3), the remaining low-order dynamics were identified as follows[§]:

$$
P_a^{\mathrm{long}} \begin{cases} \delta_e = \frac{0.67}{0.02s+1}\delta_{e_c} \\ \delta_{\mathrm{DLC}} = \frac{0.94}{0.05s+1}\delta_{\mathrm{DLC}_c} \\ \delta_{\mathrm{pl}} = 0.98\delta_{\mathrm{pl}_c} \end{cases} \qquad P_a^{\mathrm{lat}} \begin{cases} \delta_a = \frac{0.67}{0.12s+1}\delta_{a_c} \\ \delta_r = \frac{0.74}{0.07s+1}\delta_{r_c} \end{cases} \tag{4}
$$

The sinusoidal responses of the elevator and aileron actuator models are shown in Figs. 6 and 7, respectively, as gray lines. It is confirmed that the nonlinearities and uncertain factors of the actual

[§]The aileron and rudder models differ from those in [9], because the actuator systems had been repaired.

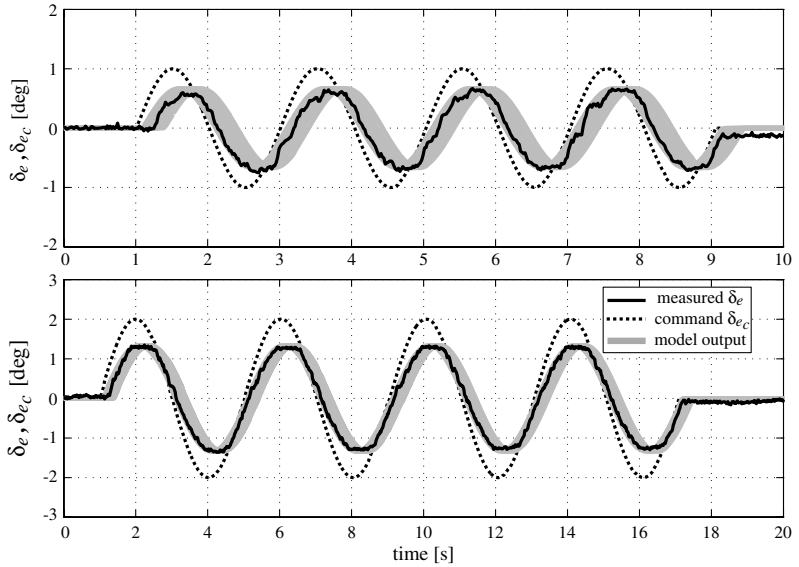

Fig. 6 Elevator response to sinusoidal input; "model output" denotes the simulation results of a system $(0.67/(0.02s+1))e^{-sT_e}$, with T_e in Eq. (3), using "command δ_{e_c}" as its input.

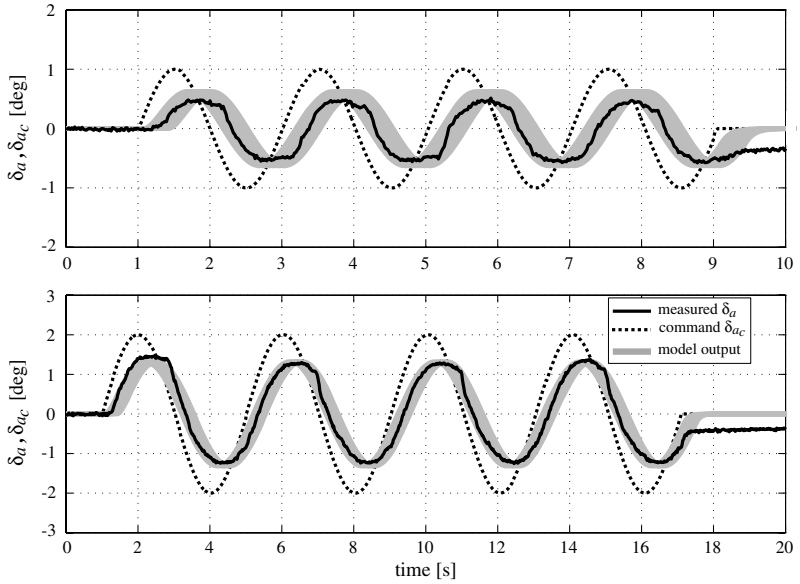

Fig. 7 Aileron response to sinusoidal input; "model output" denotes the simulation results of a system $(0.67/(0.12s+1))e^{-sT_a}$, with T_a in Eq. (3), using "command δ_{a_c}" as its input.

responses are successfully covered by the uncertainties of our models.

The uncertain dead times in Eq. (3) are approximated by first-order Padé approximations, similar to [9,13], i.e., $(-T_{\text{delay}}s/2+1)/(T_{\text{delay}}s/2+1)$ with $T_{\text{delay}} \in [T_{\min}, T_{\max}]$, and represented using a linear fractional transformation, denoted as $\text{LFT}(\delta_d, P_{\text{delay}})$, with a scalar uncertainty δ_d satisfying $|\delta_d| \le 1$ and the following P_{delay}:

$$P_{\text{delay}} \begin{cases} \dot{x}_d = A_d x_d + B_{d_1} w_d + B_{d_2} u_d \\ z_d = C_{d_1} x_d + D_{d_{11}} w_d + D_{d_{12}} u_d \\ y_d = C_{d_2} x_d + D_{d_{21}} w_d + D_{d_{22}} u_d \end{cases} \tag{5}$$

in which

$$\begin{bmatrix} A_d & B_{d_1} & B_{d_2} \\ C_{d_1} & D_{d_{11}} & D_{d_{12}} \\ C_{d_2} & D_{d_{21}} & D_{d_{22}} \end{bmatrix} = \begin{bmatrix} -(1/T_{\min}+1/T_{\max}) & 1 & 2(1/T_{\min}+1/T_{\max}) \\ -(1/T_{\min}-1/T_{\max}) & 0 & 2(1/T_{\min}-1/T_{\max}) \\ 1 & 0 & -1 \end{bmatrix}$$

Using these preliminaries, P in Fig. 4 is represented as in Fig. 8, in which A/C and P_a, respectively, denote the linearized aircraft motion models for the longitudinal or lateral-directional motions and the actuator model, i.e., P_a^{long} or P_a^{lat} in Eq. (4). Here, P_d and Δ_d are defined as P_d^{long} and Δ_d^{long} [Eq. (6)] or P_d^{lat} and Δ_d^{lat} [Eq. (7)]:

$$\begin{cases} P_d^{\text{long}} = \text{diag}(P_{d_e}, P_{d_{\text{DLC}}}, P_{d_{\text{pl}}}), \\ \Delta_d^{\text{long}} = \text{diag}(\delta_e, \delta_{\text{DLC}}, \delta_{\text{pl}}), |\delta_e| \le 1, |\delta_{\text{DLC}}| \le 1, |\delta_{\text{pl}}| \le 1 \end{cases} \tag{6}$$

$$\begin{cases} P_d^{\text{lat}} = \text{diag}(P_{d_a}, P_{d_r}), \\ \Delta_d^{\text{lat}} = \text{diag}(\delta_a, \delta_r), |\delta_a| \le 1, |\delta_r| \le 1 \end{cases} \tag{7}$$

in which P_{d_e}, $P_{d_{\text{DLC}}}$, $P_{d_{\text{pl}}}$, P_{d_a}, and P_{d_r}, respectively, denote the corresponding system P_{delay}, i.e., Eq. (5) of elevator, DLC flap, power lever, aileron, and rudder, with $T_{\min}$ and $T_{\max}$ being set as the corresponding values in Eq. (3).

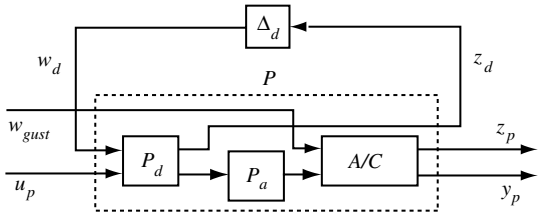

Fig. 8 Block diagram for plant *P*.

2. Feedback Controller

Because $u_a = u_i + u_g$ and $w_a = w_i + w_g$ hold, there exist direct terms from u_g to u_a and from w_g to w_a. In addition, the control devices cannot follow command signals instantaneously, because of actuator dynamics, i.e., strictly proper actuator models and delays. Consequently, the longitudinal feedback controller cannot suppress gust effects on MuPAL-α motions in the high-frequency range, and so gust suppression was applied only in the middle- and low-frequency ranges. Furthermore, it was found that the peak gains from wind gust to pitch angle could not be well suppressed by the initial design. Considering these factors, the weighting function W_1 for longitudinal motions was set as

$$W_1^{\text{long}}(s) = \text{diag}(W_{11}(s), W_{12}(s), W_{13}(s)) \tag{8}$$

in which $W_{11}(s)$, etc., are defined as follows using a parameter γ_{long}, which is to be maximized:

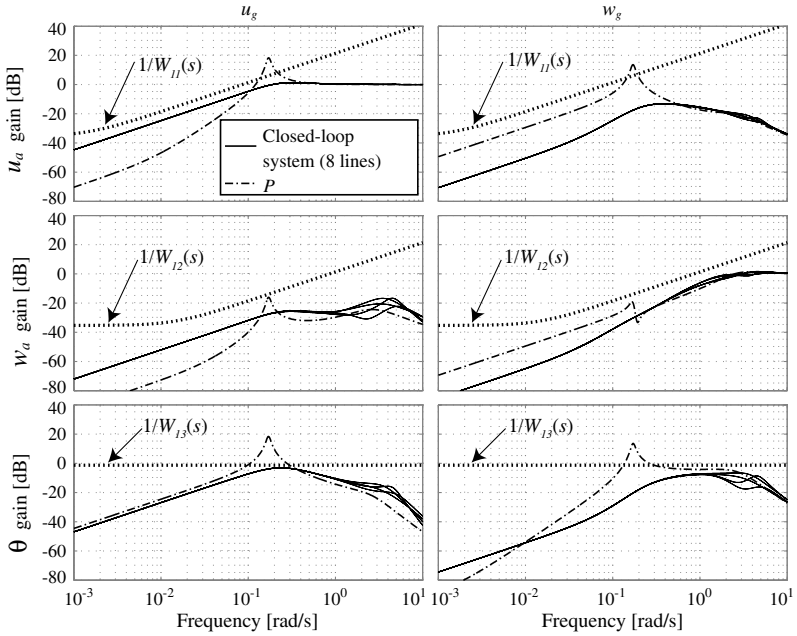

Fig. 9 Gain plots from gust to controlled output for longitudinal motions.

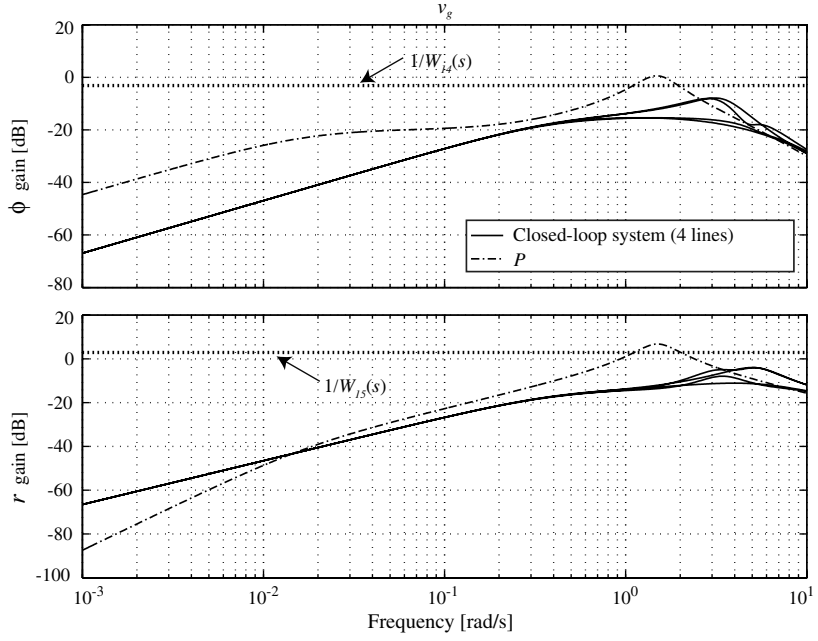

Fig. 10 Gain plots from gust to controlled output for lateral-directional motions.

$$W_{11}(s) = \frac{10\gamma_{\text{long}}}{4000/\gamma_{\text{long}}s + 1} \qquad W_{12}(s) = \frac{10\gamma_{\text{long}}}{400/\gamma_{\text{long}}s + 1}$$
$$W_{13}(s) = 0.2\gamma_{\text{long}}$$

Their gain properties, with the suboptimal γ_{long}, are shown in Fig. 9.

On the other hand, as there are no direct terms from v_g to ϕ and r, the weighting function W_1 for lateral-directional motions was given as a constant and set as

$$W_1^{\text{lat}}(s) = \text{diag}(W_{14}(s), W_{15}(s)), \qquad W_{14}(s) = \gamma_{\text{lat}}$$
$$W_{15}(s) = 0.5\gamma_{\text{lat}} \tag{9}$$

in which γ_{lat} is a design parameter to be maximized. Considering that the peak gains from v_g to ϕ and r, for the uncontrolled motions of MuPAL-α, are 1.07 and 2.02, respectively, i.e., the peak gain of ϕ from v_g is about half that of r, the coefficient matrix of W_1 was set as in Eq. (9).

We first attempted to design static feedback controllers using the method presented in [9], in which the cone complementarity linearization algorithm [14] is applied, but it was found to be very difficult for static feedback controllers to suppress gust effects. A second-order feedback controller and a first-order feedback controller were, therefore, designed for the longitudinal and lateral-directional motions, respectively. The obtained γ_{long} and γ_{lat} are 5.83 and 1.44, respectively, and the state-space matrices of the obtained K, i.e., $[A\ B; C\ D]$, are given as follows for K^{long} and K^{lat}, respectively:

$$\left[\begin{array}{cccccc}
-3.6959\times10^{-2} & 9.6682\times10^{-3} & -8.3320\times10^{-3} & -0.18536 & 0.66516 & 1.0412 \\
-2.0286\times10^{-2} & -2.4938\times10^{-2} & 4.2525\times10^{-2} & -0.20615 & -1.1088 & -2.3672 \\
-8.5681\times10^{-2} & -0.15210 & 1.4221\times10^{-3} & 1.3535\times10^{-3} & 0.54841 & 0.15450 \\
-0.54114 & 0.33180 & 1.8741\times10^{-2} & 2.1664\times10^{-2} & -1.4482 & -7.3417 \\
2.3542 & -3.0131 & -6.7244\times10^{-3} & 1.6248\times10^{-2} & 2.8118 & -7.8337
\end{array}\right]$$
$$\left[\begin{array}{ccccc}
-5.4435 & 5.4484\times10^{-2} & 0.99224 & 0.45717 & 0.61959 \\
-0.12273 & -2.0335\times10^{-3} & 0.45461 & 1.1560 & 0.59872 \\
-0.20396 & 8.3013\times10^{-3} & 0.24105 & -8.8993\times10^{-2} & 1.9563
\end{array}\right] \tag{10}$$

The following are confirmed from Eq. (10): the direct term of K^{long} has large gains, e.g., −7.3417 from θ to δ_{DLC}; on the other hand, the direct term of K^{lat} does not have such large gains; i.e., the maximum gain is 1.9563 from r to δ_r. This property is consistent with our statements, in Sec. I, on the difficulty of gust suppression of longitudinal motions.

To confirm performance, Figs. 9 and 10 show the gain plots from gust to controlled output for the longitudinal and the lateral-directional motions, respectively. Although the plots mostly overlap, eight lines and four lines, respectively, for the longitudinal and lateral-directional motions of the closed-loop system are plotted showing the combinations of maximum and minimum delays for each control input. For reference, $1/W_{11}(s)$, $1/W_{12}(s)$, $1/W_{13}(s)$, $1/W_{14}(s)$, and $1/W_{15}(s)$, using the suboptimal γ_{long} and γ_{lat}, are also shown.

Figure 10 confirms that gust suppression for lateral-directional motions is well achieved, because the peak gains are well suppressed. Figure 9 confirms the following: the frequency range over which the gain from u_g to u_a is unity for the closed-loop system is almost the same as that for the uncontrolled MuPAL-α, the same claim also holds for the gain from w_g to w_a, and other peak gains are well suppressed compared with the uncontrolled MuPAL-α. We therefore decided to use the feedback controllers given in Eq. (10).

Controller performance was also examined by numerical simulations. The results are omitted, here, because they are almost the same as those obtained from HIL simulations, which are shown in the next section.

Table 6 Performance defined by W_2^{long}

Frequency, rad/s	$1/\zeta(\omega)$
0–0.06	<0.05
0.06–0.7	<0.1
0.7–1.7	<0.2
1.7–2.0	<0.23

Table 7 Performance defined by W_2^{lat}

Frequency, rad/s	$1/\zeta(\omega)$
0–0.06	<0.05
0.06–0.6	<0.1
0.6–1.3	<0.2
1.3–2.0	<0.3

3. Feedforward Controller

The nominal system for designing a feedforward controller, i.e., P_n, is the augmented system comprising the linearized aircraft motion model, the actuator model, and the nominal delay model $(-(T_{\max} + T_{\min})s/4 + 1)/((T_{\max} + T_{\min})s/4 + 1)$, using the values in Eq. (3). Weighting functions W_2, for the longitudinal and lateral-directional motions, were set as

$$W_2^{\text{long}}(s) = 9.1/(s + 0.45)I_3 \qquad W_2^{\text{lat}}(s) = 7.1/(s + 0.35)I_2 \tag{11}$$

Performance expressed as in Eq. (2), using the W_2 in Eq. (11), is given in Tables 6 and 7, respectively, for W_2^{long} and W_2^{lat}.

Table 8 Estimated robust performance, from Fig. 11

Frequency, rad/s	$1/\zeta(\omega)$
0–0.06	<0.05
0.06–0.5	<0.1
0.5–0.9	<0.2
0.9–1.2	<0.3
1.2–1.4	<0.4

Table 9 Estimated robust performance, from Fig. 12

Frequency, rad/s	$1/\zeta(\omega)$
0–0.06	<0.05
0.06–0.6	<0.1
0.6–1.3	<0.2
1.3–1.8	<0.3
1.8–2.0	<0.36

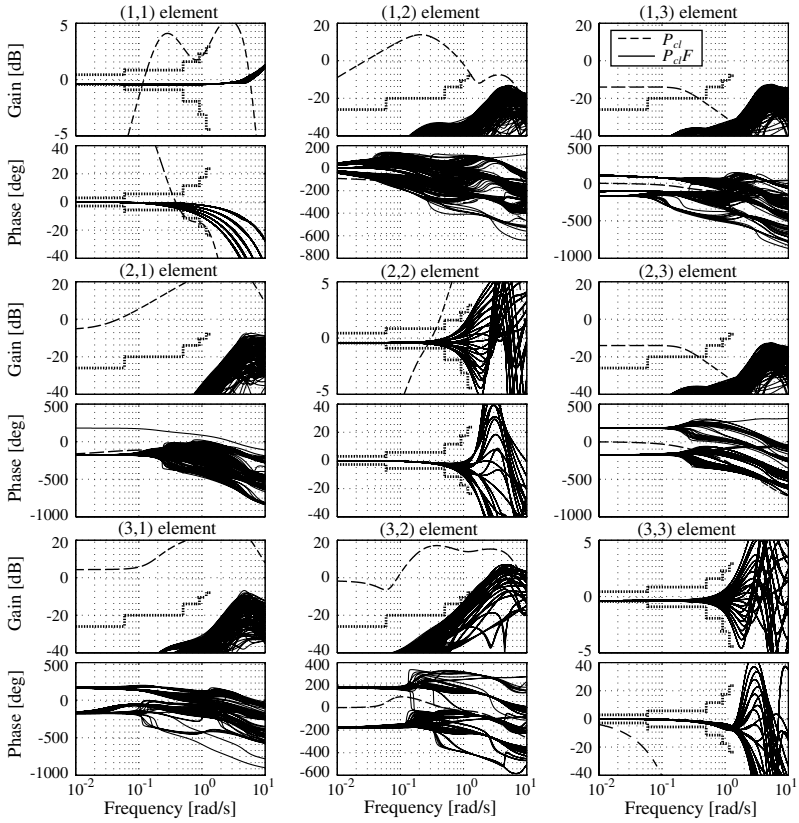

Fig. 11 Bode plots from w_2 to z_p for longitudinal motions; dotted lines represent estimated robust performance bound in Table 8.

Using the weighting functions W_2, full-order feedforward controllers were designed that guarantee the performance specified in Tables 6 and 7 for nominal systems. The designed controllers were of 15th order for the longitudinal motions, and of 11th order for the lateral-directional motions.

The robust performance of the designed controllers against the uncertain delays in Eq. (3) was checked by the gridding method; i.e., the uncertainty ranges were gridded linearly (five points for the delay intervals for both longitudinal and lateral-directional motions), and controller performance was checked at all combinations of the gridding points. The Bode plots of the systems from w_2 to z_p in Fig. 5 are shown in Figs. 11 and 12 for the longitudinal and lateral-directional motions, respectively. Bode plots of the closed-loop system $P_{\rm cl}$, with the nominal delay $(T_{\max} + T_{\min})/2$, are also shown for reference.

The robust performance expressed as in Eq. (2), estimated from Figs. 11 and 12, are shown in Tables 8 and 9, respectively. The bound of the estimated robust performance is also shown as dotted lines, in Figs. 11 and 12.

Unfortunately, the a posteriori estimated robust performance does not satisfy the design requirements in Tables 6 and 7. However, it is confirmed from Figs. 11 and 12 that the designed feedforward

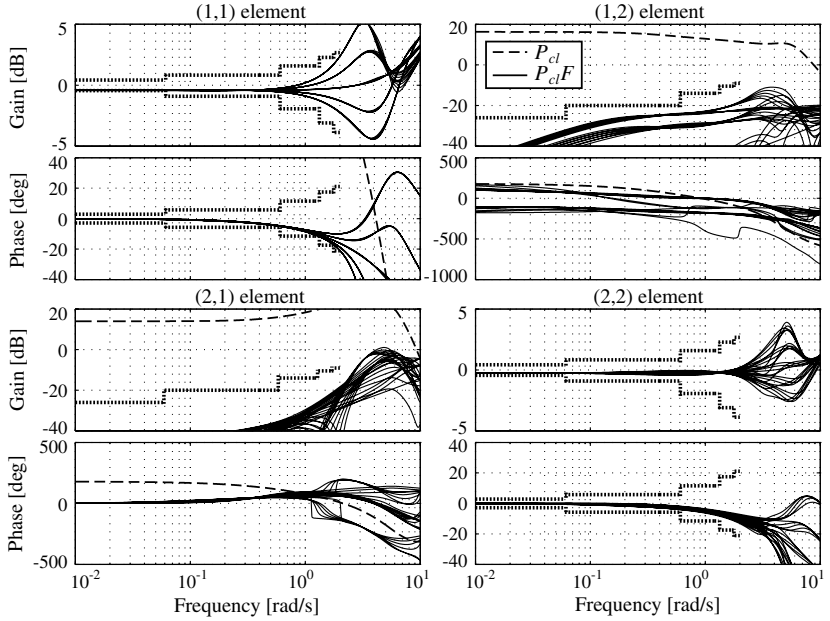

Fig. 12 Bode plots from w_2 to z_p for lateral-directional motions; dotted lines represent estimated robust performance bound in Table 9.

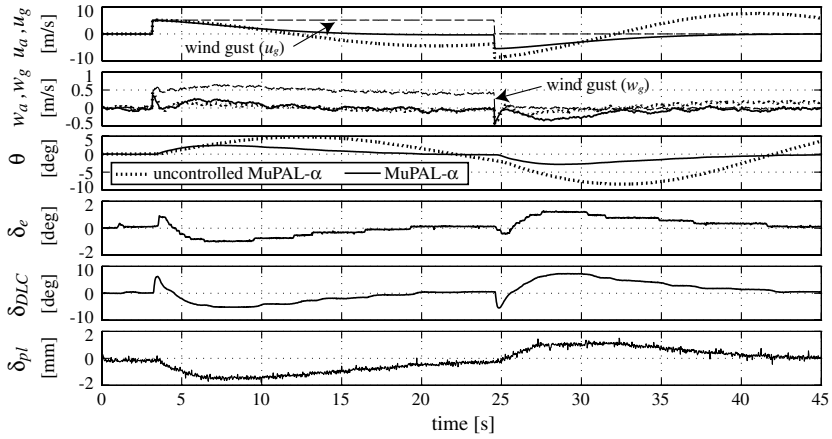

Fig. 13 HIL simulation result of gust suppression for longitudinal motions.

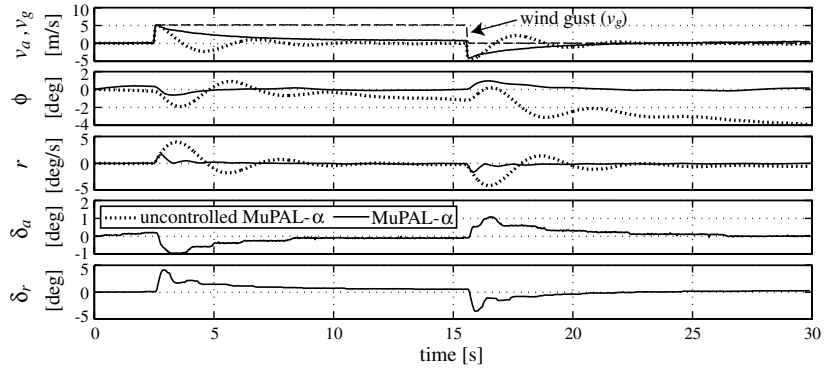

Fig. 14 HIL simulation result of gust suppression for lateral-directional motions.

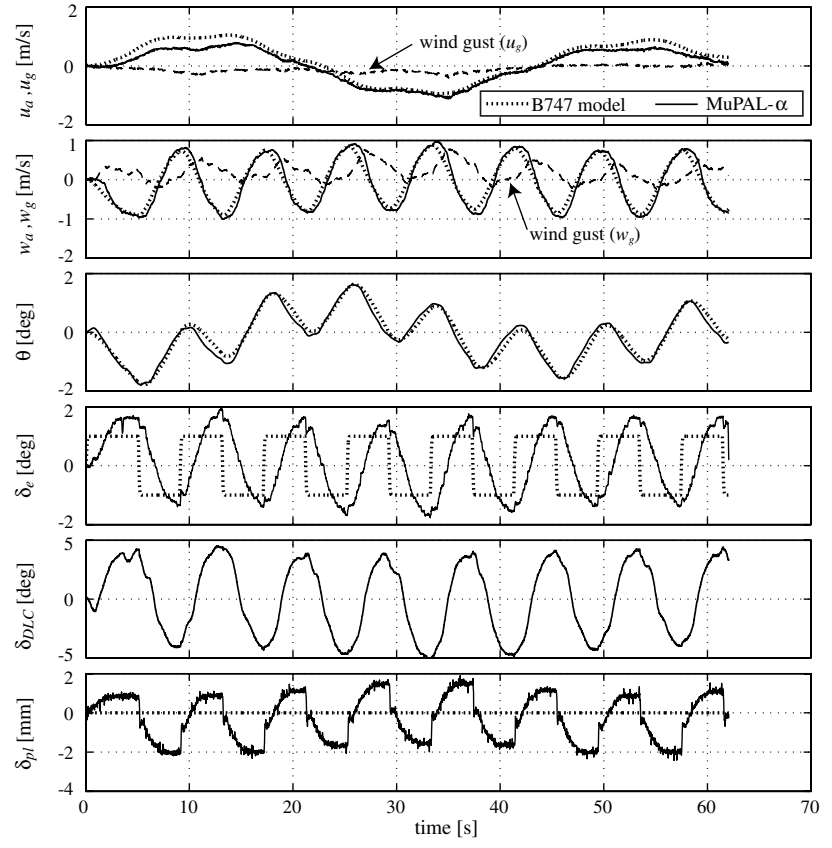

Fig. 15 Elevator doublets for B747 model.

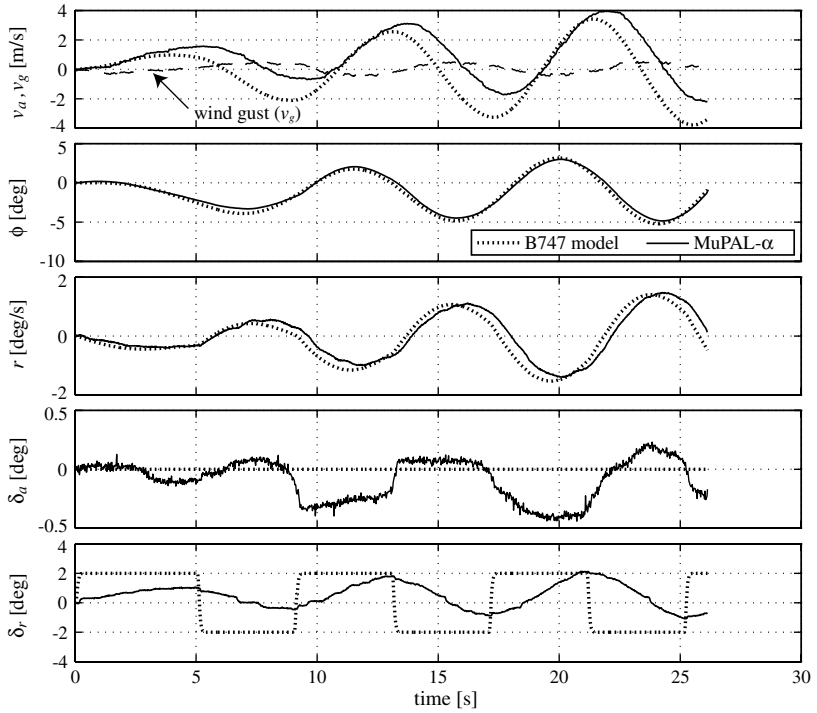

Fig. 16 Rudder doublets for B747 model.

controllers work as inverse systems for their supposed plant systems, comprising the uncertain plant P and the designed feedback controller K in the low-frequency range, especially in [0, 1] rad/s. That is, the designed feedforward controllers can realize a range of maneuverability with low-frequency inputs.

III. Experiment Results

The designed flight controllers were implemented in MuPAL-α's flight control computer. For both longitudinal and lateral-directional motions, the controllers F and K were implemented as discrete-time systems after discretization using a bilinear transform with 0.02 s. Noise reduction filters, $F_1 = (1/(0.03s + 1)^3)\mathbf{I}$ for u_m and $F_2 = (1/(0.02s + 1))\mathbf{I}$ for y_p, were implemented as discrete-time systems after discretization using a zero-order hold with 0.02 s.

To verify the variable maneuverability, the following three models were used as the target aircraft model: 1) B747 model [15], steady level flight at a true air speed of 67.4 m/s at an altitude of 0 m in the landing configuration, without stability augmentation system (SAS); 2) regional jet model, steady level flight in the approach configuration without SAS; and 3) artificial aircraft model,

$$\begin{cases} u_a = 0.1/(s+1)^2\delta_{\mathrm{pl}} \\ w_a = (180/\pi)/(s+1)^2\delta_e \\ \theta = (180/\pi)/(4s+1)^2\delta_x \\ \phi = -(180/\pi)/(s+1)^2\delta_a \\ r = -(180/\pi)/(s+1)^2\delta_r \end{cases}$$

The units in the artificial aircraft model are as follows: u_a m/s, δ_{pl} mm, w_a m/s, δ_e rad, θ deg, ϕ deg, δ_a rad, r deg /s, and δ_r rad. In this model, an additional pilot input δ_x was used to control pitch angle. The additional input was operated by onboard system operators, because the pilot only had conventional controls (column, power lever, wheel, and pedal).

Engine data were not provided in the B747 and regional jet models, and so engine dynamics were modeled as first-order systems in both cases. The time constants of the engine models for the B747 and the regional jet models were set as 5 and 2 s, respectively, and the gains were appropriately defined.

The models were implemented in the flight control computer as discrete-time systems after discretization using a zero-order hold with 0.02 s.

A. Hardware-in-the-Loop Simulations

Similar to [9], HIL simulations were carried out to confirm controller performance before actual flight experiments. These simulations confirmed that the designed controllers achieved gust suppression as well as a wide range of maneuverability, without requiring redesign.

As the HIL simulation results confirming the variable maneuverability are similar to the flight test results, only HIL simulation results confirming gust suppression performance with step gusts are shown in Figs. 13 and 14, for the longitudinal and lateral-directional motions, respectively (only horizontal gusts were simulated, because the HIL simulation program does not allow input of vertical wind gusts). The uncontrolled MuPAL-α motions, calculated offline using recorded gust data and zero control inputs, are also shown for reference. Figure 13 confirms that the phugoid mode was well suppressed, and all deviations due to gust settled within about 15 s. Figure 14 confirms that all deviations due to gust settled within about 3 s. Thus, it was confirmed that the designed controller for lateral-directional motions well suppresses the effects of gust.

B. Flight Experiments

Flight experiments were carried out after HIL simulations. The results shown next were obtained on 19 and 24 June 2009. The estimated wind gusts ($u_g = u_a - u_i$, etc.) are also shown for reference in the figures. Although these experiments could not be conducted during a single flight, due to weather conditions and a fuel problem, nothing was changed other than the model M in Fig. 3b.

Figures 15–17 show flight test results for the B747 model. In Fig. 15, elevator doublets are input to excite the short-period mode of the model. In Fig. 16, rudder doublets are input to excite the Dutch roll mode. In Fig. 17, the pilot was required to climb at a steady rate and to make a doublet roll input. In all figures, only small

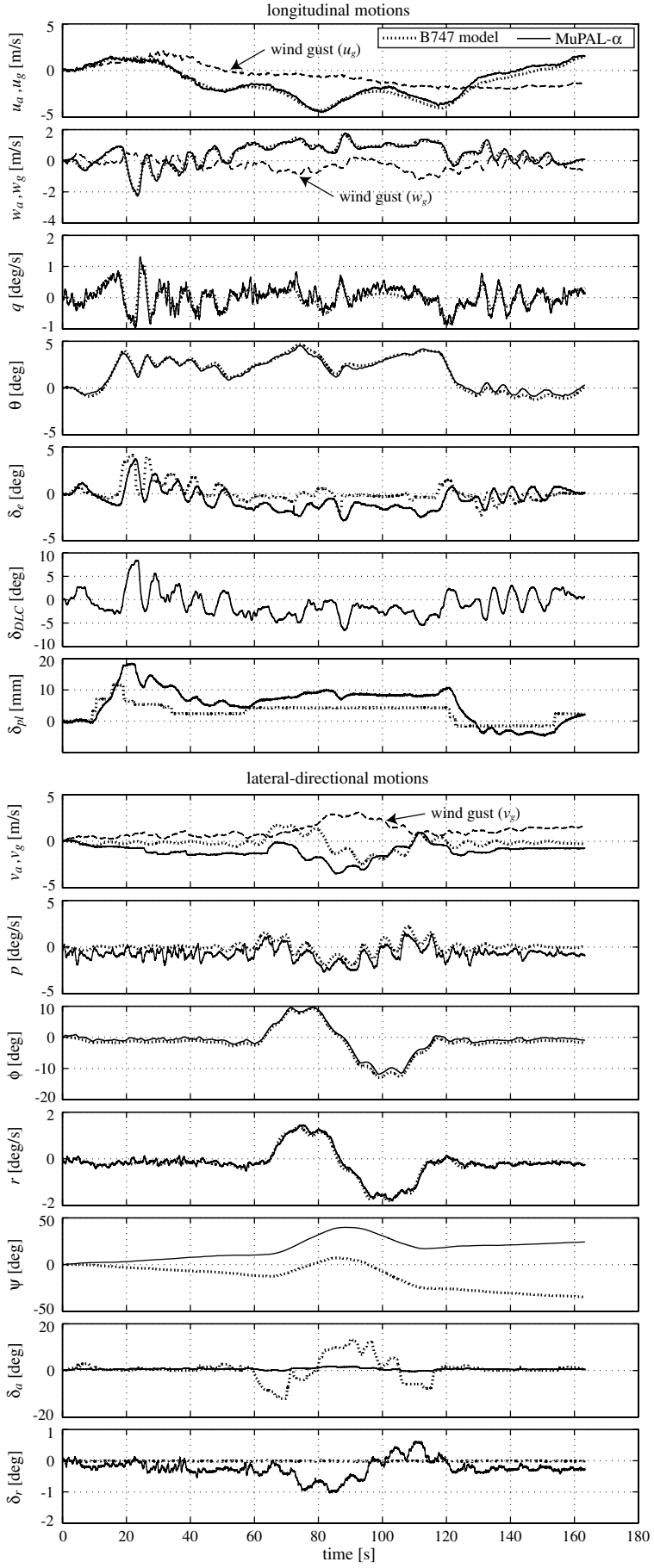

Fig. 17 Flight result using B747 model.

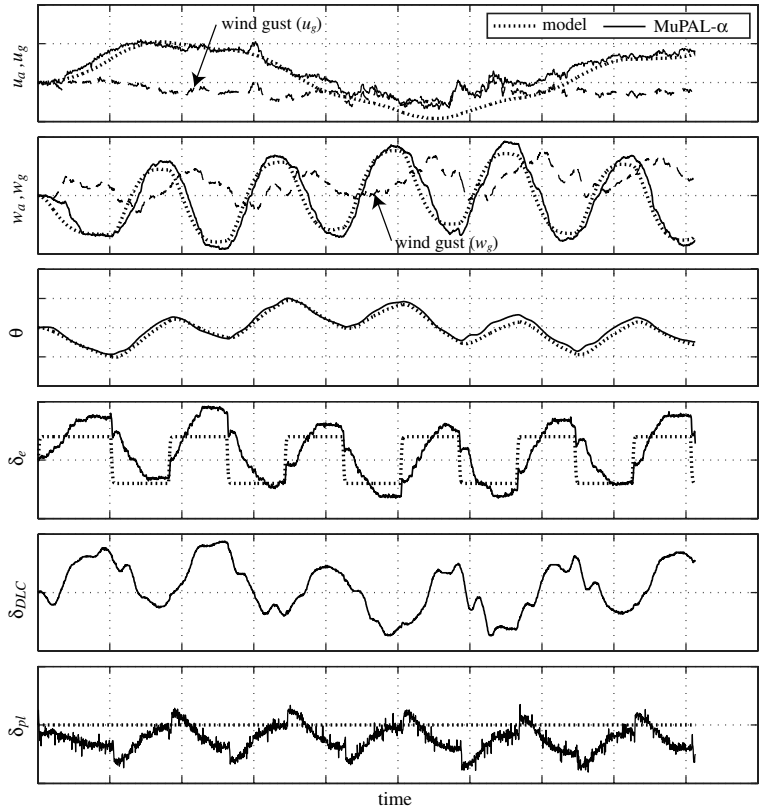

Fig. 18 Elevator doublets for regional jet model.

discrepancies are found between the controlled output of MuPAL-α and the output of the B747 model, i.e., u_a, w_a, and θ for the longitudinal motions, and ϕ and r for the lateral-directional motions. Thus, it was confirmed that MuPAL-α with our controllers well matches the maneuverability of the B747 model.

Figures 18–20 show the results for the regional jet model (the values and units cannot be released, for reasons of confidentiality). In Fig. 18, elevator doublets are input to excite the short-period mode of the model. In Fig. 19, rudder doublets are input to excite the Dutch roll mode. In Fig. 20, the pilot was required to execute a task similar to that in Fig. 17. In all figures, there are only small discrepancies between the controlled output of MuPAL-α and the output of the model, confirming that MuPAL-α with our controllers mimics well the maneuverability of the regional jet model.

Figure 21 shows the results for the artificial aircraft model. Apart from during the interval 210–240 s, it is confirmed that MuPAL-α

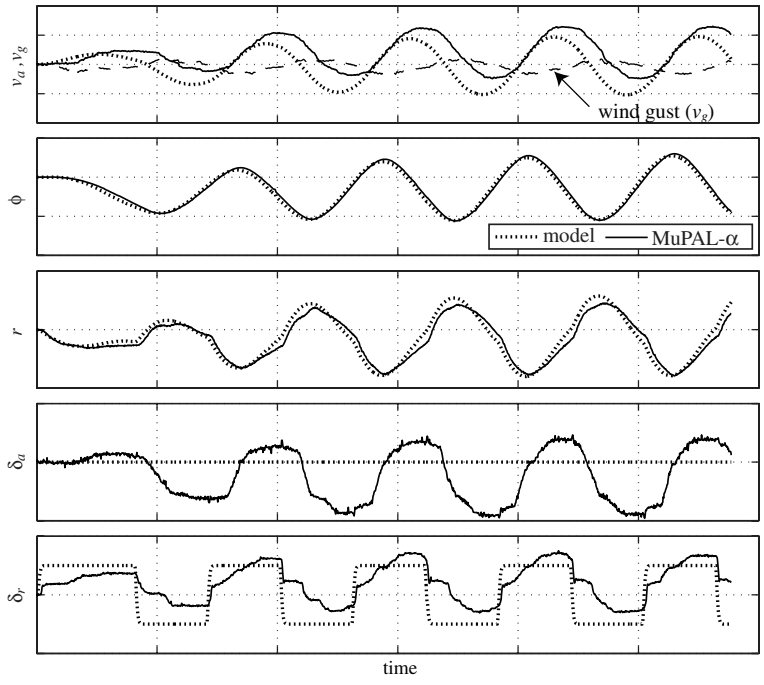

Fig. 19 Rudder doublets for regional jet model.

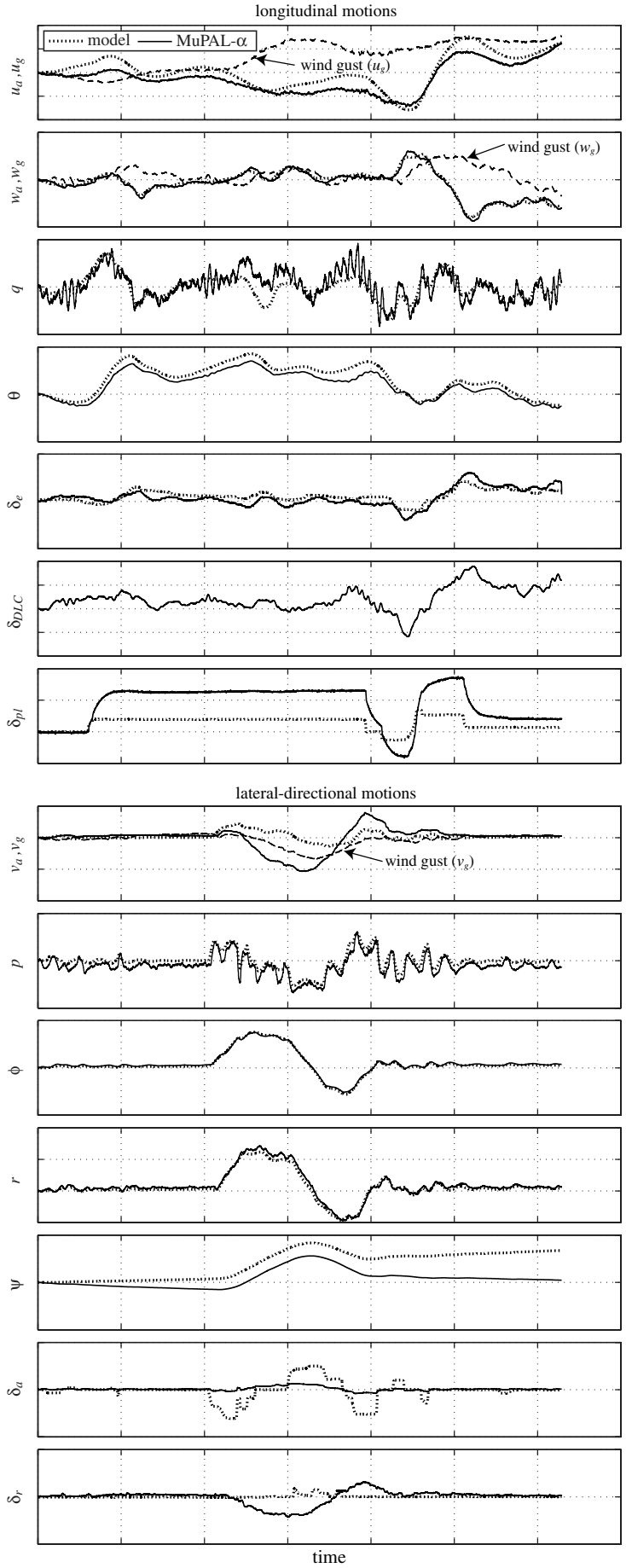

Fig. 20 Flight result using regional jet model.

with our controllers well mimics the dynamics of the artificial aircraft model, because there exist only very small discrepancies between the controlled output of MuPAL-α and the output of the model. In the interval 210–240 s, sideslip angle reached about 15°, which is the most probable cause of the large discrepancies in the longitudinal motion outputs.

As mentioned previously, the flight controllers were not changed, but only the model M was replaced. Nonetheless, the prescribed maneuverability was realized even when the model was far from conventional, as shown in Fig. 21. These flight results, therefore, demonstrate that MuPAL-α with our controllers can realize a wide range of maneuverability.

On the other hand, gust suppression could not be clearly confirmed from the flight experiments, due to the relatively calm weather conditions. However, it is inferred from the following that gust suppression in real conditions is well achieved:

1) There are only a few discrepancies in u_a, and there are very small discrepancies in other outputs under some gusts.

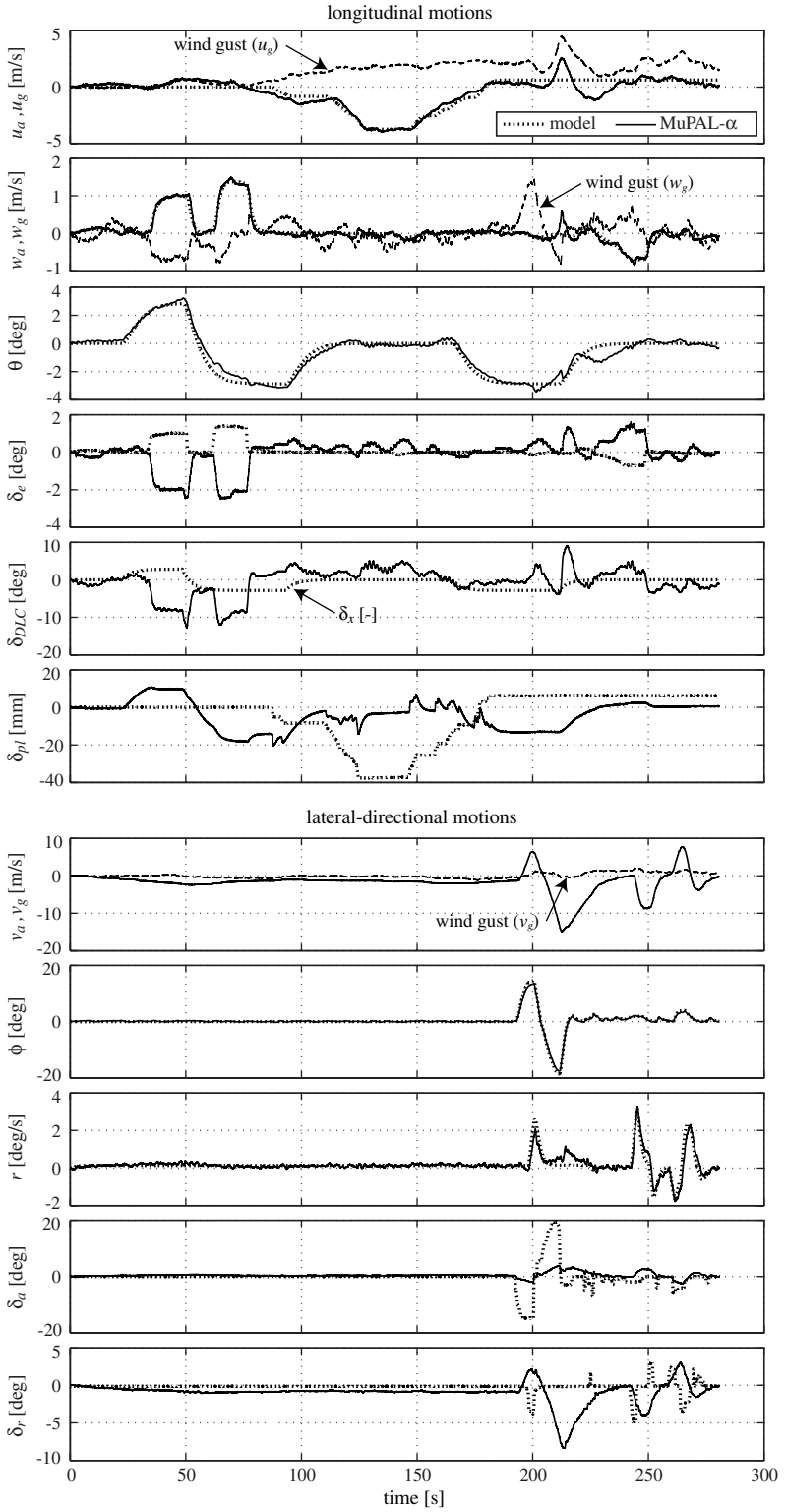

Fig. 21 Flight result using artificial aircraft model.

2) It is confirmed that the maneuverability realized in the flight experiments is very similar to that in HIL simulations, in which gust suppression was well achieved.

IV. Conclusions

This paper reports the verification results of flight controllers for an in-flight simulator (IFS), MuPAL-α. The design requirements are twofold: suppression of the effects of gusts on IFS motions and the realization of a wide-range maneuverability without redesign of the flight controllers. Using a previously proposed design method, the applicability of which had been confirmed only for lateral-directional motions, flight controllers were designed for the longitudinal and lateral-directional motions of MuPAL-α. Hardware-in-the-loop (HIL) simulations and flight experiments, using the designed controllers and a variety of aircraft models, confirmed that our flight controllers achieved gust suppression as well as a wide range of maneuverability without redesign of controllers.

As gust suppression of controller design for the longitudinal motions of MuPAL-α is more difficult than for its lateral-directional motions, it is inferred that a similar claim holds for the gust response realization problem, which is another design requirement for IFS flight controllers. However, it has not yet been clarified whether or not the claim indeed holds or what type of gust responses can be realized with MuPAL-α. These topics are future works to be investigated.

Appendix: State-Space Matrices of MuPAL-α Motions

The state-space matrices of A/C, in Fig. 8, i.e.,

$$\begin{bmatrix} A & B \\ C & D \end{bmatrix}$$

are given as

$$\begin{bmatrix}
-0.019174 & 0.17540 & -5.4804 & -9.7752 & 0.024921 & -0.019174 & 0.17540 & 0.43421 & 0.34910 & 0 \\
-0.18163 & -1.1476 & 67.818 & -0.78485 & -4.7690\times10^{-3} & -0.18163 & -1.1476 & -5.3754 & -7.5216 & 0 \\
7.4341\times10^{-3} & -0.074534 & -1.9984 & 5.7215\times10^{-3} & 5.5662\times10^{-4} & 7.4341\times10^{-3} & -0.074534 & -4.5708 & 0.98283 & 0 \\
0 & 0 & 1.0000 & 0 & 0 & 0 & 0 & 0 & 0 & 0 \\
0 & 0 & 0 & 0 & -2.2133 & 0 & 0 & 0 & 0 & 3.1267 \\
1.0000 & 0 & 0 & 0 & 0 & 1 & 0 & 0 & 0 & 0 \\
0 & 1.0000 & 0 & 0 & 0 & 0 & 1 & 0 & 0 & 0 \\
0 & 0 & 0 & 57.296 & 0 & 0 & 0 & 0 & 0 & 0 \\
1 & 0 & 0 & 0 & 0 & 1 & 0 & 0 & 0 & 0 \\
0 & 1 & 0 & 0 & 0 & 0 & 1 & 0 & 0 & 0 \\
0 & 0 & 1 & 0 & 0 & 0 & 0 & 0 & 0 & 0 \\
0 & 0 & 0 & 1 & 0 & 0 & 0 & 0 & 0 & 0
\end{bmatrix}$$

for the longitudinal motions and as

$$\begin{bmatrix}
-0.18920 & 5.4538 & 9.7748 & -68.950 & -0.18920 & 0 & 3.1800 \\
-0.060800 & -3.9900 & 0 & 1.3190 & -0.060800 & -11.800 & 1.3050 \\
0 & 1.0000 & 0 & 0.080809 & 0 & 0 & 0 \\
0.028000 & -0.035300 & 0 & -0.50100 & 0.028000 & 0.39700 & -2.4500 \\
0 & 0 & 57.296 & 0 & 0 & 0 & 0 \\
0 & 0 & 0 & 57.296 & 0 & 0 & 0 \\
1 & 0 & 0 & 0 & 1 & 0 & 0 \\
0 & 1 & 0 & 0 & 0 & 0 & 0 \\
0 & 0 & 1 & 0 & 0 & 0 & 0 \\
0 & 0 & 0 & 1 & 0 & 0 & 0
\end{bmatrix}$$

for the lateral-directional motions, in which the input is $[\, w_{\text{gust}}^T \quad u_p^T \,]^T$, and the output is $[\, z_p^T \quad y_p^T \,]^T$.

Acknowledgment

The authors greatly appreciate the kind support of Mitsubishi Heavy Industries, Ltd., for providing their regional jet model.

References

[1] Weingarten, N., "History of in-Flight Simulation at General Dynamics," *Journal of Aircraft*, Vol. 42, No. 2, 2005, pp. 290–298. doi:10.2514/1.4663

[2] Shafer, M., "In-Flight Simulation Studies at the NASA Dryden Flight Research Facility," NASA TM-4396, Washington, D.C., 1992.

[3] Motyka, P., Rynaski, E., and Reynolds, P., "Theory and Flight Verification of the TIFS Model-Following System," *Journal of Aircraft*, Vol. 9, No. 5, 1972, pp. 347–353. doi:10.2514/3.58991

[4] Hanke, D., and Lange, H., "Flight Evaluation of the ATTAS Digital Fly-by-Wire/Light Flight Control System," *Proceedings of ICAS 16th Congress*, ICAS, Jerusalem, 1988, pp. 866–876.

[5] Henschel, F., and Chetty, S., "Flight Control System Design for an in-Flight Simulator," *Journal of Guidance, Control, and Dynamics*, Vol. 12, No. 3, 1989, pp. 351–356. doi:10.2514/3.20415

[6] Komoda, M., Kawahata, N., Tsukano, Y., and Ono, T., "VSRA in-Flight Simulator: Its Evaluation and Applications," AIAA Paper 1988-4605-CP, Sept. 1988.

[7] Masui, K., and Tsukano, Y., "Development of a New in-Flight Simulator MuPAL-α," AIAA Paper 2000-4574, Aug. 2000.

[8] Sato, M., "Design Method of Flight Controllers for in-Flight Simulators," Ph. D. Dissertation, Univ. of Tokyo, Tokyo, 2009.

[9] Sato, M., and Satoh, A., "Simultaneous Realization of Handling and Gust Responses: In-Flight Simulator Controller Design," *Journal of Guidance, Control, and Dynamics*, Vol. 31, No. 6, 2008, pp. 1545–1560. doi:10.2514/1.36713

[10] Yoshikawa, T., and Sugie, T., "Filtered Inverse Systems," *International Journal of Control*, Vol. 43, No. 6, 1986, pp. 1661–1671. doi:10.1080/00207178608933566

[11] Giusto, A., and Paganini, F., "Robust Synthesis of Feedforward Compensators," *IEEE Transactions on Automatic Control*, Vol. 44, No. 8, 1999, pp. 1578–1582. doi:10.1109/9.780425

[12] Sato, M., "Inverse System Design for LPV Systems Using Parameter-Dependent Lyapunov Functions," *Automatica*, Vol. 44, No. 4, 2008, pp. 1072–1077. doi:10.1016/j.automatica.2007.08.013

[13] Ohno, M., Yamaguchi, Y., Hata, T., Takahama, M., Miyazawa, Y., and Izumi, T., "Robust Flight Control Law Design for an Automatic Landing Flight Experiment," *Control Engineering Practice*, Vol. 7, No. 9, 1999, pp. 1143–1151. doi:10.1016/S0967-0661(99)00085-4

[14] Ghaoui, L., Oustry, F. and AitRami, M., "A Cone Complementarity Linearization Algorithm for Static Output-Feedback and Related Problems," *IEEE Transactions on Automatic Control*, Vol. 42, No. 8, 1997, pp. 1171–1176. doi:10.1109/9.618250

[15] Heffley, R., and Jewell, W., "Aircraft Handling Qualities Data," NASA CR-2144, Washington, D.C., Dec. 1972.